Tuning the defects density in additively manufactured fcc aluminium alloy via modifying the cellular structure and post-processing deformation

P Snopiński, Ondrej Hilšer, Jiří Hajnyš

Tuning the defects density in additively manufactured fcc aluminium alloy via modifying the cellular structure and post-processing deformation

P. Snopiński[1,*], Ondrej Hilšer[2], Jiří Hajnyš[2]

[1] *Department of Engineering Materials and Biomaterials, Silesian University of Technology, 18A Konarskiego Street, 44-100 Gliwice, Poland;*

[2] *Faculty of Mechanical Engineering, VSB-TU Ostrava, 17. Listopadu 2172/15, 708 00 Ostrava, Czech Republic*

**corresponding author e-mail: przemyslaw.snopinski@polsl.pl*

Abstract

In this study, using an L-PBF AlSi10Mg alloy with different microstructural properties, the typical structural defects caused by severe plastic deformation are investigated by scanning electron microscopy and high-resolution transmission electron microscopy. Microscopic characterization shows that the deformed L-PBF AlSi10Mg alloy exhibits a heterogeneous microstructure consisting of Al/Si interfaces and a high density of dislocations, stacking faults, and nanotwins. On the basis of experimental data, it is also shown that high stresses build up at the Al/Si interface due to incompatible deformation, enabling the activation of novel deformation modes that control the plastic deformation of the hard Si twin phase and amorphization in the solid state. The revealed synergy and novel deformation modes open a new horizon for the development of next-generation structural materials and provide insights into the atomically resolved structures of dislocations and GBs in nanostructured L-PBF alloys.

Keywords: AlSi10Mg, heat-treatment, severe plastic deformation, deformation mechanisms, stacking faults, deformation twins

Introduction

AlSi10Mg is a high-strength aluminum alloy mainly used in die casting (HPDC), permanent mold casting (PM), and recently in laser powder bed fusion (L-PBF) [1]. It owes its popularity to the attractive combination of mechanical properties, good castability, weldability and a low coefficient of thermal expansion. Comparing the microstructures of cast materials and those produced by the L-PBF process, it is clear that they are fundamentally different [1] [2]. The SLM process does not produce dendritic structures, but rather ultrafine metastable cellular structures with the accompanying segregation of elements that are usually held responsible for the unprecedented mechanical properties. More importantly, this cellular structure exhibits a type of heterogeneity that favours inhomogeneous plastic deformation and hinders the movement of dislocations, contributing to a higher storage capacity of dislocations triggered by single or multiple strengthening mechanisms [3] [4] [5]. For this reason, static mechanical tensile tests on L-PBF parts have shown yield strengths (YS) of up to ~300 MPa, compared to ~150 MPa for conventionally cast parts. In view of this, L-PBF AlSi10Mg alloy can provide an alternative starting point for novel post-processing strategies based on "hierarchical defect and grain boundary engineering" to achieve better mechanical properties of metallic materials [6].

Since Zhang first printed the AlSi10Mg alloy in 2001 [7], most of the research work on this alloy has focused on densification behaviour [8], microstructure analysis [9], tensile properties [10], heat treatment [11], and post-processing technologies [12]. To meet the stringent requirements of the industry, considerable efforts were also made to improve the

mechanical properties by modifying the morphology of the cellular microstructure of the L-PBF AlSi10Mg alloy [13] [14]. It has been found that heat treatments can alter the microstructure that controls strength, with the cellular structure disintegrating wholly or partially into a coarse network of Si rich particles and the Si rich nanoprecipitates undergoing either a spheroidization or a dissolution process depending on the holding time and temperature [15] [16].

In addition, a change in Si morphology has been shown to affect dislocation storage capacity, which is related to the loss of load-bearing capacity of silicon due to the loss of interconnectivity of eutectic Si [17]. It was found that more geometrically necessary dislocations (GNDs) and statistically stored dislocations (SSDs) accumulate at the fully cellular Al/Si interface than at the partially cellular or noncellular one, because the mobile dislocations can cross the micrometre-sized grains much more easily than the semicontinuous (in the case of partially cellular) or fully cellular (in the case of cellular) ones [18]. In other words, the carrying capacity of silicon decreases with the loss of continuity of the Si network and its coarsening. In view of this, manipulation of the cellular morphology of silicon appears as a novel strategy that can lead to a novel structural response and activation of additional deformation modes, i.e., deformation twins and stacking faults, as well as an efficient heterodeformation-induced strain hardening effect under severe plastic deformation conditions [19] [20] [21]. It is also plausible to assume that the activation of additional deformation modes might be easier in materials with grains reduced to the nanoscale. However, in the case of L-PBF AlSi10Mg, this effect has hardly been studied in detail. This research gap limits our understanding of the deformation mechanisms of L-PBF alloys and is essential to push the limits of strength-ductility.

In this work, the microstructure of L-PBF AlSi10Mg alloy was modified based on the following considerations: (1) The L-PBF AlSi10Mg samples were heat- treated at 280 and 320 ºC for 9 minutes to obtain different cellular Si morphology. (2) The sample with coarser Si and a more disconnected Si network was post-processed with ECAP at 100 ºC. It was hoped that the more disconnected network and coarser Si would reduce the dislocation storage capacity; on the other hand, a lower deformation temperature would inhibit dynamic recovery (DRV). (3) The sample with finer Si and more interconnected Si network was post-processed with ECAP at 150 ºC. It was hoped that the more interconnected network and finer Si would increase the dislocation storage capacity. On the other hand, a higher deformation temperature would allow a more dynamic microstructure (DRV) to be obtained.

The objective of this study is to find out if there exist any interplay between microstructural properties (Si phase morphology) and deformation mechanisms. To the best of author knowledge, this work represents a novelty, as there are no published research papers that address in such detail the nanoscale plastic deformation mechanisms of the AlSi10Mg alloy subjected to severe plastic deformation using the equal channel angular pressing (ECAP) process.

Methodology

In this article, the gas atomized AlSi10Mg powder produced by Sigma Aldrich was used to fabricate the samples by selective laser melting (SLM) method. Before being used for 3D printing, the large and sintered particles were separated by sieving the powder through a sieve with a mesh size of 63 µm.

A rectangular samples of dimensions 15 × 15 × 60 mm were fabricated using a TruPrint 1000 system and optimized L-PBF parameters, i.e. a laser power of 175 W, a laser scanning velocity of 1.4 m/s, powder-bed thickness of 0.02 mm.

The samples obtained by L-PBF were then post-processed according to the following heat treatment schemes:

- Low temperature annealing for 9 minutes at 280 °C (sample HT280),
- Low temperature annealing for 9 minutes at 320 °C (sample HT320),

Although the heat treatment changed the Si morphology, it also aimed to partially remove residual stresses and improve technological plasticity.

Following heat treatment, the working samples were pressed once through the 90º ECAP die (introducing an equivalent strain of ε = ~1) according to the following schemes:

- sample HT280 -> ECAP at 150ºC (sample HT280E150),
- sample HT320 -> ECAP at 100ºC (sample HT320E100),

The microstructure was then analysed by a combination of optical microscopy, transmission electron microscopy (TEM) using a S / TEM TITAN 80-300 microscope and by scanning electron microscopy (SEM) using a Zeiss Supra 35 instrument equipped with a EDAX EBSD system. EBSD analysis was performed with an accelerating voltage of 20 kV, step size of 0.03 μm, and a tilt angle of 72°. ATEX software was used to analyse the EBSD data and generate orientation maps, as well as to calculate the GND density based on the KAM values according to methods published elsewhere [22]. X-ray diffraction analysis was performed using a PANalytical X'Pert Pro diffraction system (Malvern Panalytical Ltd., Royston, UK) equipped with a CoKα radiation source.

Results

Microstructure analysis

Figure 1 shows the initial heterogeneous microstructures of the heat-treated samples photographed in the X-Y plane (cross sections perpendicular to the build direction). The SEM microstructural images of the etched surfaces show three distinct zones formed due to exposure to different temperature gradients on the laser scan track during the L-PBF process, Fig. 1 (a) and (c).

(1) MP fine, characterized by a fine cellular microstructure,

(2) MP coarse, where the width of the cells was almost twice as large as in the fine zones,

(3) Heat-affected zone (HAZ), characterized by a branched morphology of Si phase.

According to Figs. 1 (b) and (d) the cellular eutectic Si separates the primary Al matrix and the two samples have a similar cell size. It is also noticeable that holding at higher temperatures causes a stronger disintegration of the Al/Si eutectic network and its coarsening (thickening).

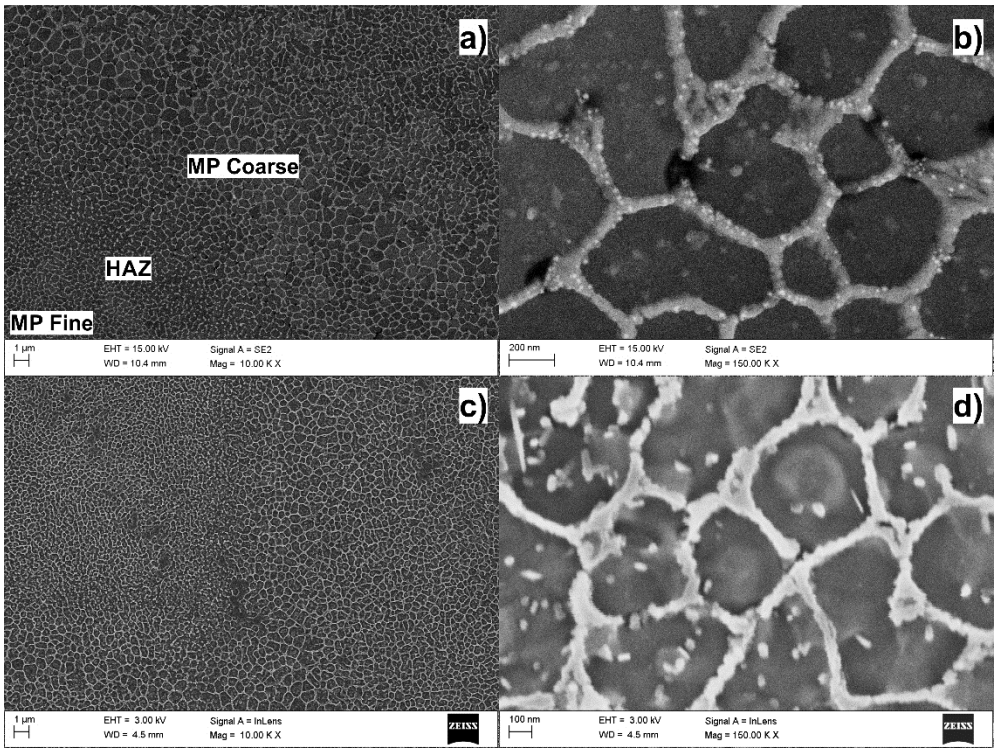

Figure 1. Microstructure of the heat treated AlSi10Mg sample a), b) and c) HT280 sample, d), e) and f) HT320 sample

The microstructural analysis performed with the scanning electron microscope shows that the studied samples have maintained their heterogeneous microstructure after ECAP processing. As can be seen, the first level of microstructural heterogeneity is represented by semicircular melt pools (Fig. 2 (a) and (c)), in which three different zones were identified: the heat-affected zone (HAZ), the coarse ('MP coarse') and the fine ('MP fine') zones, while the second heterogeneity is represented by cellular Si-rich eutectic networks.

Fig. 2(b) and (d) show higher magnification microscopic images comparing cellular Si morphology in the MP fine zone MP (which is usually considered a representative zone for such comparisons). As can be seen, partial decay and spheroidisation of the eutectic Si network occurred in both samples. It is also noticeable that HT280E150 has many precipitates generally less than 20 nm in diameter within the cellular structure (Fig. 2(b)). This indicates that the ECAP treatment induced a high dislocation density, which provides a good opportunity for pipe diffusion or nucleation of precipitates on dislocation cores [23].

From the comparison of Fig. 2(b) and (d), it can also be concluded that the higher deformation temperature promotes the globularization of the Si network, since the HT280E150 sample has a thicker Si network. It can be speculated that holding at high temperature leads to higher diffusion, resulting in spheroidization phenomena in the Si network and precipitation of supersaturated Si atoms within the cells. This hypothesis agrees well with the results published by Li and other authors, who studied the precipitation of Si atoms in the form of nano- or micrometric particles from supersaturated solid solutions in an SLM-processed AlSi10Mg alloy [24].

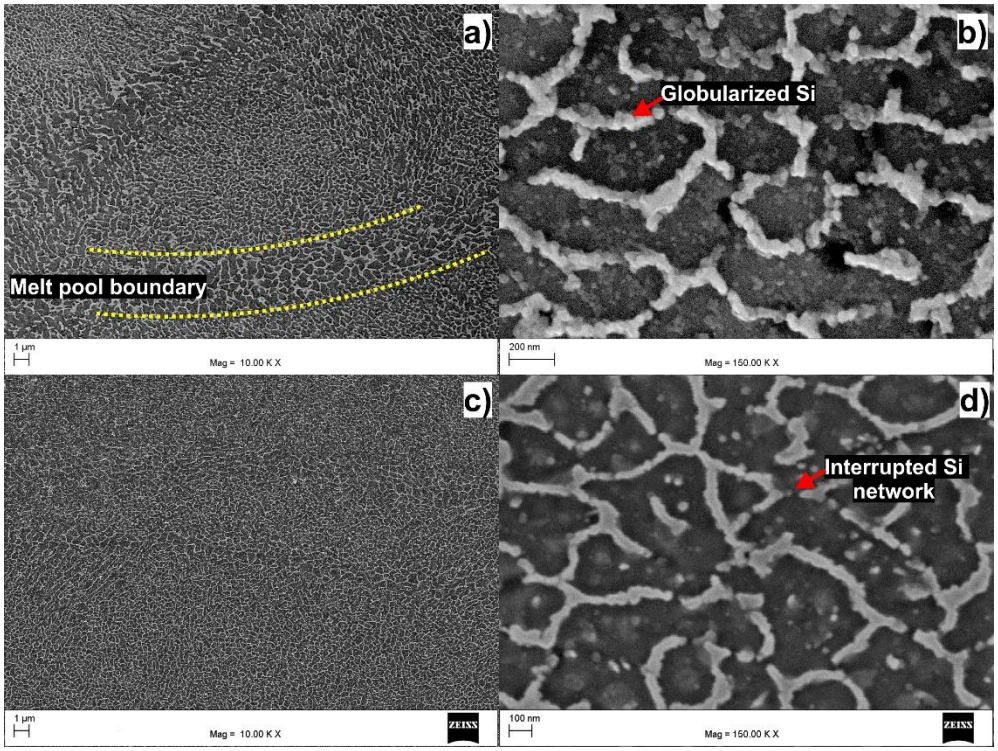

Figure 2. Microstructure of the ECAP processed samples a), b) and c) HT280E150 sample, d), e) and f) HT320E100 sample

In the next step of investigation, the structural defects resulting from ECAP were analysed via electron backscatter diffraction (EBSD). It can be seen in Fig. 3(a) and (e) that EBSD detects areas of higher lattice distortion (areas of low pattern quality), confirming the presence of multiple dislocation walls and subgrain boundaries as well as the crucial role of Al/Si interfaces in the grain refinement process

It is evident that more surface crystalline defects (grain and subgrain boundaries) were formed in the HT320E100 sample than in the HT280E150 sample. According to the data in Table 1, the grain size was reduced to 0.35 µm and 0.24 µm in HT280E150 and HT320E100 samples, respectively. Moreover, it is noticeable that more grain boundaries were converted into high-angle grain boundaries (HAGBs) after ECAP processing of the HT320 sample, so that the proportion of boundaries with misorientation angle θ > 15 º accounted for ~68% of the total GBs, confirming a more intense grain subdivision process in the HT320E100 sample (Fig. 3(c) and (g)). It can be speculated that a lower deformation temperature allowed the introduction of higher dislocation densities; because ECAP samples are inevitably statically annealed during deformation, resulting in faster recovery; therefore, LAGBs transform into HAGBs much faster thus forming a finer microstructure.

The map of GND distribution in Figs. 3(d) and (h) confirms that the GNDs pile up in front of the Al/Si interface region (which is obviously due to the compensation of strain and stress incompatibilities between the Al/Si interfaces) and shows the effectiveness of the heterodeformation mechanism between the Al/Si interfaces. However, in the case of sample HT320E100, the GND distribution also extends into the grain interior, resulting in an average $\rho_{GND} = 1.67*10^{15}m^{-2}$. It is also worth noting that the GND density in sample HT320E100 is even higher than in sample HT280E150, which is probably due to the higher deformation temperature leading to the relaxation of the strain gradients [25] (due to the dynamic recovery at the Al/Si interfaces during ECAP).

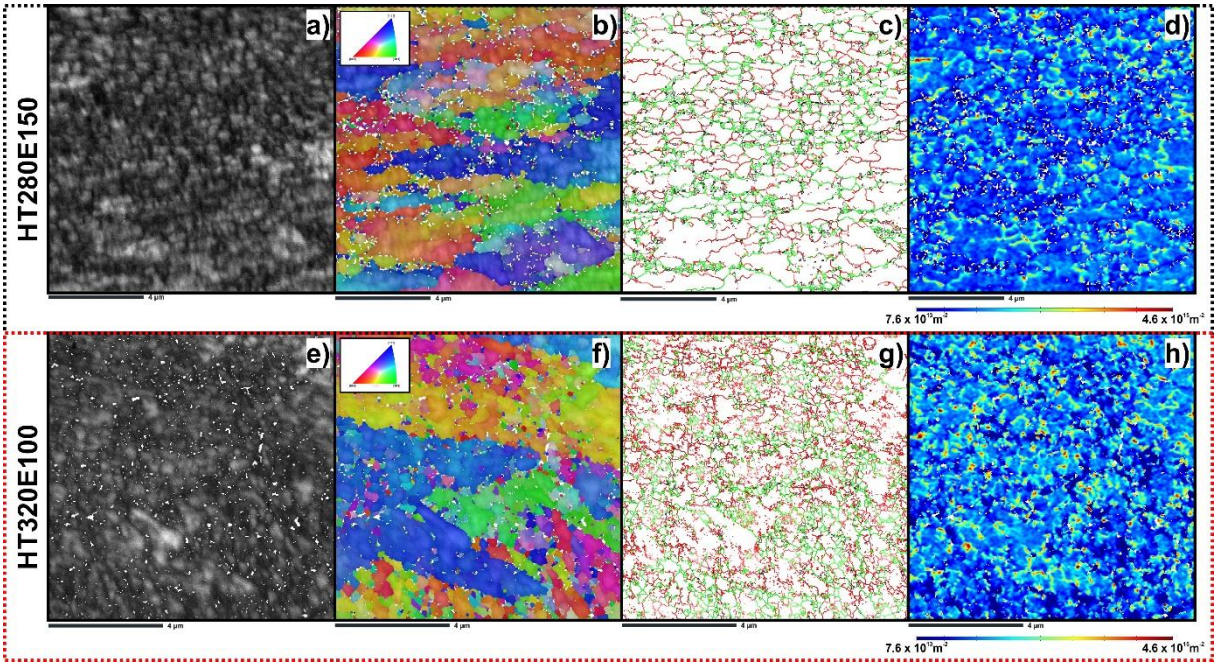

Figure 3. Results of the EBSD analysis a) and e) band contrast map, b) and f) IPF-Z map, c) and g) grain boundary map (HAGBs, with misorientations greater than 15° were marked by green lines, LAGBs, with misorientations 2°<θ<15° were marked by green lines), d) and h) GNDs map

Table 1. Microstructural parameters of ECAP-processed samples obtained from EBSD analysis

Sample ID	f_{LAGBs}, %	f_{HAGBs}, %	Grain size, µm
HT280E150	47.1	52.9	0.35
HT320E100	32.4	67.6	0.24

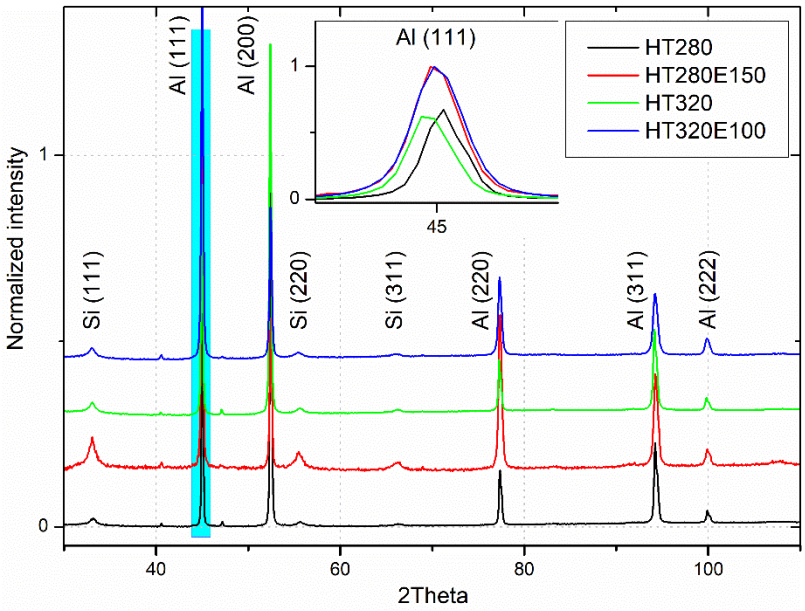

Figure 4. XRD profiles of investigated samples

Fig. 4 shows the XRD patterns of the heat-treated and ECAP samples. The inset is the magnified view of the pattern from 44 to 46º. X-ray diffraction (XRD) analysis shows the existence of two crystalline α-Al and Si-I phases. The significant broadening of the (111) peak reveals grain refinement along with high lattice distortion (higher defect density). For the quantitative analysis of dislocation density, the XRD measurements were combined with the Rietveld analysis (see data in Table 2) [26]. It can be seen that the ρ_{XRD} values are on the order of 1×10^{14} m^{-2}, which is much higher than $\times 10^{9}$ or $\times 10^{10}$ m^{-2} for conventional cast or wrought metals [27]. Such high ρXRD values for a heat treated metal can be attributed to the presence of preexisting dislocations formed due to the high cooling rate during the L-PBF process. It was also confirmed that the dislocation density after the ECAP process increased to $2.92*10^{14}$ m^{-2} and $3.46*10^{14}m^{-2}$ for HT280E150 and HT320E100, respectively.

Table 2. Evolution of microstructural parameters from XRD analysis

Sample ID	Lattice parameter, Å	Dislocation density, (m^{-2})
HT280	4.0446	$1.93*10^{14}$
HT320	4.0505	$1.47*10^{14}$
HT280E150	4.0477	$2.92*10^{14}$
HT320E100	4.0485	$3.46*10^{14}$

To investigate the main defects in the microstructure of the ECAP samples at higher resolution, TEM was performed. Figure 5 (a) and (f) shows the main microstructural features of HT280E150 sample imaged in the ED-TD plane. It can be seen that the microstructure of both samples consists of subgrains with a size of 200 to 300 nm, which is consistent with the EBSD analysis presented above. It is also noticeable that numerous dislocations have formed and accumulated, indicating that the deformation of the aluminum phase is controlled by the dislocation slip. BF-DF TEM micrographs at higher magnification (Figs. 5(b) and (c)) and the high-resolution TEM micrographs (Fig. 5(d) and (e)) show more details of the substructure of the HT280E150 sample. As you can see, the subgrain boundary consists of network of screw dislocation and the measured misorientation angle between subgrains is about 4.7º. It can be assumed the sub-grain boundary forms by the recombination of screw dislocations and edge dislocations during the dynamic recovery process [28].

Aluminium alloys have high SFE, so screw dislocations can slide crosswise, which allows faster dynamic recovery to compensate for strain hardening during ECAP deformation [29] [30]. According to Al-Fadhalah et al. this leads to a faster evolution of the UFG equilibrium structure as the grain refinement process is mainly controlled by the climbing of edge dislocations and the cross-slip of screw dislocations [31]. Fig. 5(d) documents the existence of twin bands within the Si precipitates. It also implies that at high strain levels silicon particles are also able to accommodate some deformation via stacking fault and twinning. Interestingly, the Fast Fourier transform pattern (with polycrystalline rings) of a boundary region (highlighted in Fig. 5(b)) shows the absence of a periodic structure, indicating a possible deformation-induced solid-state amorphization of the silicon phase [32].

At low magnification, sample HT320E100 shows a slightly different microstructure (Fig. 5(f)). The bright- field TEM image reveals elongated subgrains separated by an almost continuous Si network, see dashed lines. The BF-DF TEM microscopic images of the Al/Si interface at higher magnification (Figs. 5(g)-(h)) also confirm the presence of dislocation networks within the subgrains. As can be seen in Fig. 5(k), the subgrain interface consists of a network of screw dislocations. However, here the measured misorientation angle (indicative of LAGB) between two adjacent subgrains is slightly higher (~5.9º). Such LAGBs (found in both samples studied) develop from GNDs, and the underlying mechanism may be similar to that described by Wu et al [33]. Fig. 5(f) also shows that stacking faults (SFs) were formed in the Al matrix. The SFs are expected to distort the interfacial lattice and impede the movement of dislocations [34]. It is worth mentioning that the high density of SFs in the ECAP-processed sample may contribute to strain hardening to some extent. Figures 5(i) and (j) are STEM and TEM images showing the area around the cell boundaries at higher magnification. The diffuse scattering of the FFT diffractogram in Fig. 5(i) indicates the presence of similar amorphous regions as seen in Fig. 5(d). Several dislocations are also visible in this figure, confirming that high stresses have built up near the Si phase, possibly due to incompatible deformation.

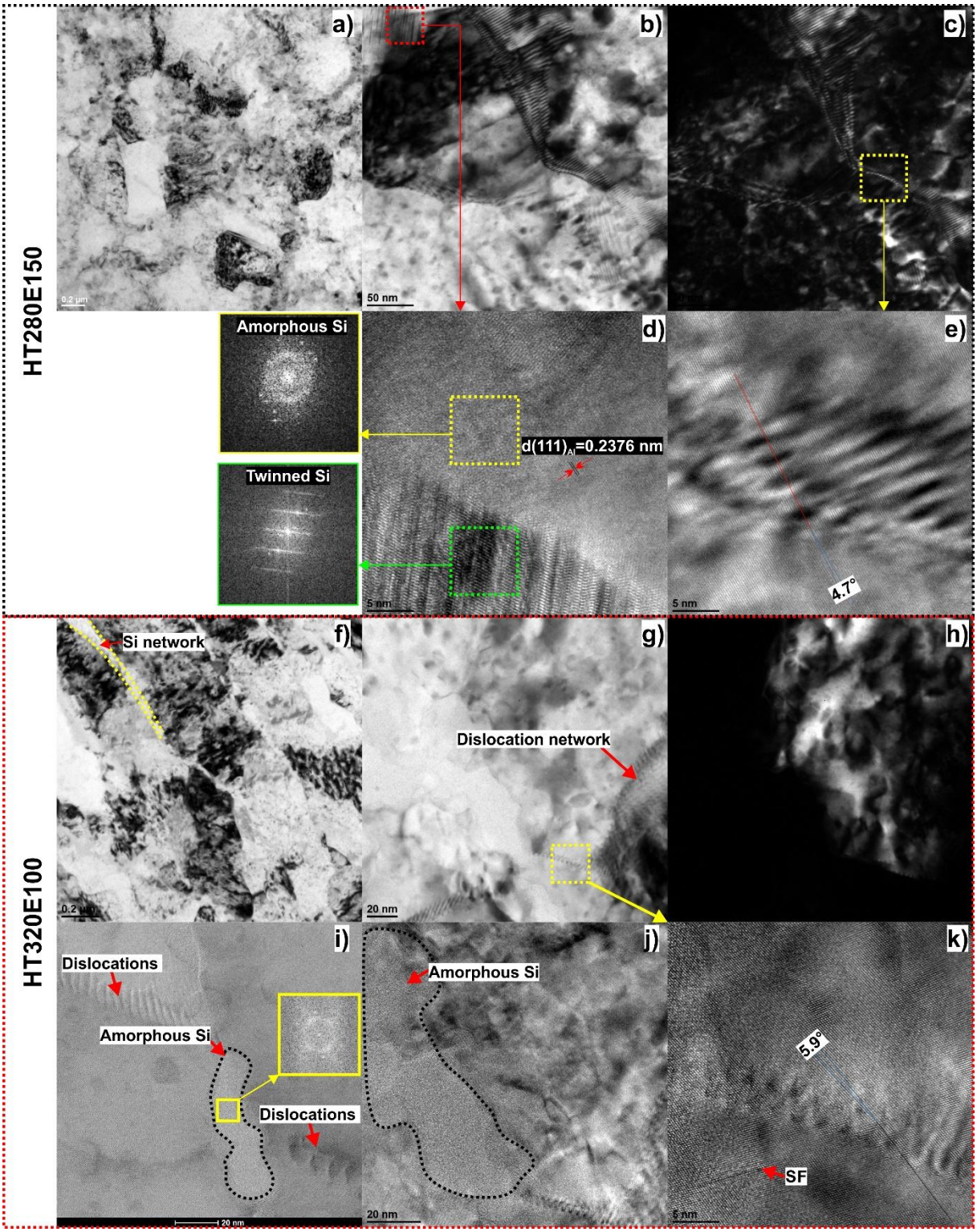

Figure 5. deformation microstructures of samples HT280E150 and HT320E100 a) low magnification image showing the general microstructure of sample HT280E150, b) and c) higher magnification brightfield and darkfield TEM micrographs, d) and e) HRTEM images showing the boundary regions highlighted in Fig. 5(b) and (c), respectively. f) Low magnification BF TEM micrograph showing a well-developed subgrain structure, g) and h) higher magnification brightfield and darkfield TEM images, i) STEM image of the Al/Si interface region with FFT showing modulated contrast typical of an amorphous structure, j) HRTEM image of the region shown in (g), k) HRTEM image of the subgrain boundary showing screw dislocations and stacking faults

Main structural defects formed after ECAP process

Deformation twins and stacking faults

Twinning is an important deformation mechanism in metals and alloys, especially in coarse-grained face-centred cubic (FCC) metals with low stacking fault energy and in nanocrystalline materials. In aluminium alloys, the formation of twins is usually considered impossible due to a relatively high stacking fault energy (SFE) [35]. However, the studied alloy contains silicon as the main alloying element, which not only reduces the redistribution of electrons on the stacking fault energy (silicon has a stacking fault energy of about 50-60 mJ/m^2) (by weakening the redistribution of electrons on the stacking fault plane), but also provides additional dislocation sources. According to Zhu et al. [36], to activate deformation twinning in FCC metals extreme conditions such as low temperature, high strain rate deformation, nanograin size, or enormous deformation in a single pass are required. Indeed, the microscopic images presented in this article show exceptional grain refinement (down to the submicron range) realised under enormous deformation conditions; therefore, it can be assumed that some main factors enabling twinning have been fulfilled.

Figure 6 shows an example of a region where multiple deformation microtwins or stacking faults have formed in an ultrafine Al matrix. Such stacking faults can refine the mean free path of dislocations, facilitating strain hardening through the dynamic Hall-Petch effect [37]. To further investigate the possible microstructural defects, part of the selected region in the HRTEM image (see the rectangular zone in Fig. 6 (a)) was analysed using the fast Fourier transform (FFT). The fringes in the FFT pattern reflect the planar defect diffraction characteristic (Fig. 6(c)), where the diffraction spots degenerate along the direction of the defect plane. From Fig. 6(d), it is clear that the defects observed in the Al matrix are extrinsic stacking faults. An interaction between SFs and dislocations can also be seen, suggesting that SFs blocks dislocation movement and thus increases the dislocation storage capacity of the aluminium matrix.

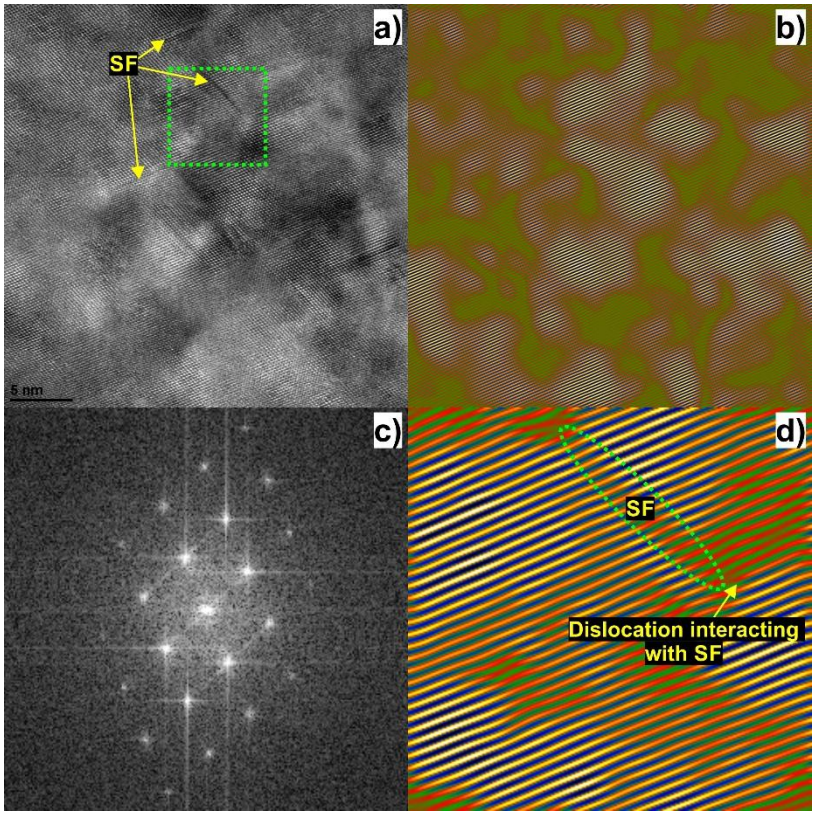

Figure 6. Results of TEM analysis a) HRTEM micrograph of the aluminium matrix, b) inverse FFT from (a), c) FFT taken from rectangular area in (a), d) inverse FFT obtained from the green rectangular area in (a)

Various mechanisms of twinning/stacking fault formation in FCC metals have been described to explain this phenomenon [38] [36] [39]. Here, it can be speculated that partial dislocations, which could originate from the Al/Si interface or grain boundary regions, promote the formation of stacking faults or "microtwins" in the aluminium matrix. According to the study by Shu et al [40], the activation of partial dislocations is easier than that of lattice dislocations when the grain size is close to a critical value. This suggests that the formation of twin/stacking faults may be the preferred mechanism in a nanocrystalline AlSi10Mg alloy.

It is also hypothesised that deformation incompatibility could lead to an increase in interfacial shear stress, resulting a decrease in effective stacking fault energy and triggering SF within the aluminium matrix. The prediction of γ_{eff} can be evaluated by measuring the width of SF from HRTEM micrographs. The relationship between the width of SF and γ_{eff} can be described as follows:

$$\gamma_{eff} = \frac{Gb^2}{4\pi} \cdot \frac{1}{d} \quad (1)$$

Where γ_{eff} is the SFE per unit area, G is the aluminium shear modulus in GPa, b is the length of Burger's vector, and d is the measured average width of stacking fault formed in aluminium matrix. According to the Fig. (c,d,e) the width of SFs formed in the α-Al matrix varies from 7.6 – 10.5 nm, with an average value of about 8.2 nm. Using the equation above and following constants G = 35 GPa, b = 0.286 nm, the calculated effective stacking fault energy equals to about ~29 mJ/m^2, which is much lower than that of conventional coarse-grained aluminium alloy (122 mJ/m^2) [41].

The experimental results presented above are in good agreement with molecular dynamics simulations showing that the main deformation mechanisms of L-PBF aluminium alloys with cellular structure are dislocation slip, stacking fault, and amorphization [42], as well as with experimental data documenting the presence of SF -s within an aluminium matrix in Al-Si alloys [43]. The formation of SFs was also observed in Al-Mg-Si alloy subjected to the equal-channel angular pressing [44] and in the AlSi10Mg alloy subjected to very high cycle fatigue deformation [20].

In addition, examination of the HRTEM microphotographs reveals several planar defects - stacking faults (SF) and twins formed within the Si nanograins (Fig. 7). However, it should be mentioned here that twins and stacking faults have been observed only in sample HT320E100, which has a more continuous Si network and was deformed at lower temperature (see Figs. 2(b) and (d)). Therefore, it can be assumed that the deformation mode of the Si phase changes with increasing deformation temperature. The atomic staggering in the HRTEM and STEM images and the streaking in the corresponding FFT patterns confirm that both the identified Si-I and Si-III polymorphic phases are faulty with dislocations, stacking faults, and deformation twins that compensate for the lattice mismatch between the α-Al and Si planes.

The formation of deformation twins and stacking faults within Si particles can be explained on the basis of strain gradient theory [45]. It can be conjectured that the strain gradient between the soft and hard phases, which occurred during ECAP processing, resulted in load transfer from the plastically deformed matrix to the unyielded Si phase. As long as the load transfer occurred, the stresses between the phases also increased. When the local stress concentration exceeded the critical shear strength of Si, twin deformation occurred within the Si particles, resulting in deformation continuity from the relatively ductile α-Al matrix to the brittle eutectic Si phase [43].

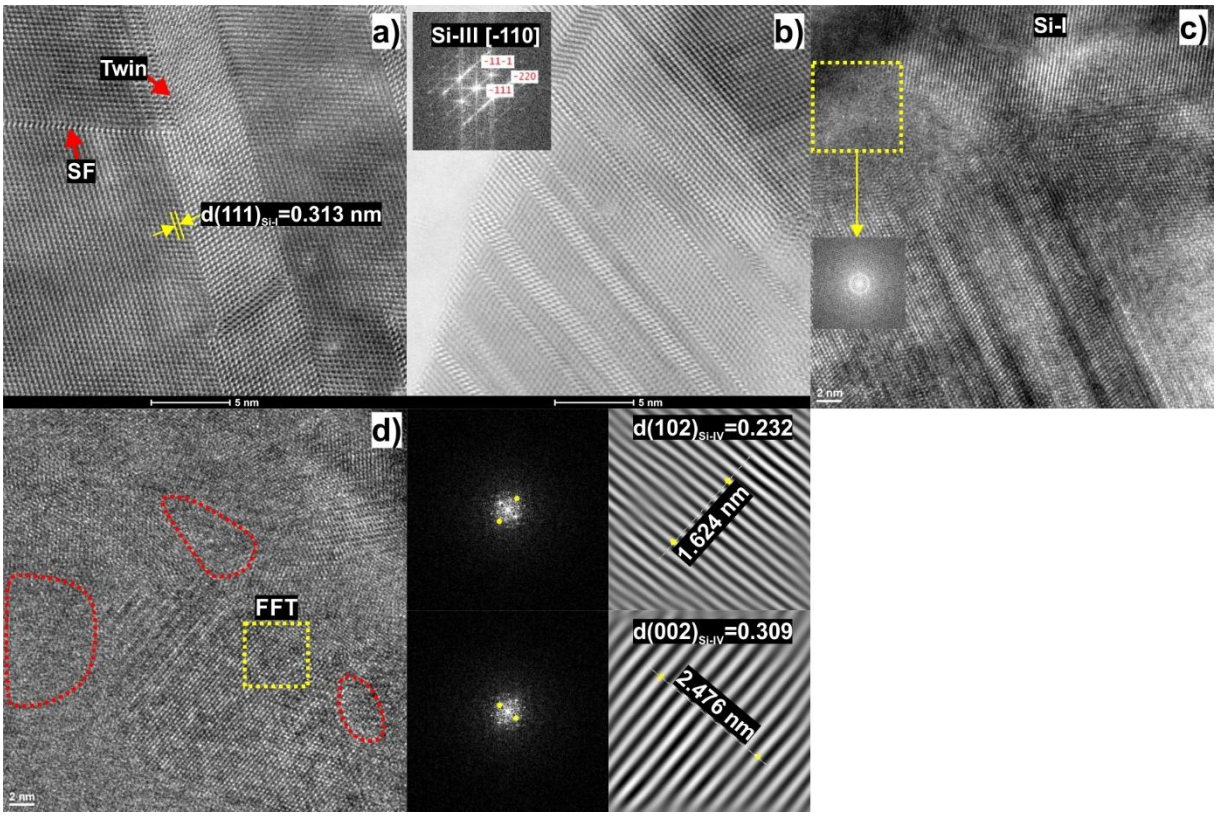

Figure 7. Main defects formed within Si particles a) and b) STEM HAADF images showing intense twining and stacking fault formation within Si-I and Si-III phases, c) and d) amorphous regions close to the Si-I and Si-IV phases, in (d)(outlined by the red dashed line regions in (d) are mostly amorphous – no long range ordering

Amorphous areas

Deformation-induced local amorphization is currently proposed as a new deformation mechanism that provides a way to dissipate the applied strain energy and effectively relieve the large stresses that arise at the heterozone interfaces [46]. In general, as strain energy (defect density) increases, elastic deformation leads to dislocation formation and motion, then twinning, then phase transformation, and finally, in the extreme case of high strain accumulation and/or high strain rate, amorphization [47] [48]. Obviously, extremely high strain is introduced into the material during ECAP deformation, so such an unusual deformation mechanism can be expected.

In Figure 7(c) and (d), the presence of amorphous layers at the boundaries of the Si crystallites is confirmed by the HRTEM images. Interestingly, it is also documented that three polymorphic forms of silicon exist in the microstructure of the studied alloy. The first is the fcc Si-I (also detected by XRD analysis), the second is the bcc Si-III Kasper phase and the third is Si-IV. Indeed, previous studies have shown fracture of Si under indentation in a cast Al-18Si alloy, as well as evidence for amorphization of Si and phase transformation of diamond-cubic Si to bcc-Si and rhombohedral Si [49], so it can be assumed here that amorphous domains (detected by TEM) were formed by phase transformation rather than rapid solidification.

The mechanism of the above mentioned Si phase transformation in the L-PBF AlSi10Mg alloy can be described as follows. During the ECAP process, high stresses (in the range of 9 - 16 GPa) build up near the Si phase due to incompatible deformation, inducing the phase transformation from fcc Si-I to β Si- II (which is associated with a volume decrease of 22% compared to the Si-I phase). Depending on the pressure release rate, the unstable β Si- II phase transforms into a rhombohedral (R8) Si- XII or body-centred cubic (BC8) Si-III [50], and then from the Kasper phase to Si-IV. It should be mentioned here that the phase transformation into a Si-III phase is accompanied by an increase in volume (the Si-III phase

has a larger structural volume than Si- II). This transformation causes a kind of "explosion" leading to its refinement [51]. At the same time, the grain boundaries, which are not only sources of defects, but also their sinks, absorb vacancies by storing the excess non-equilibrium free volume and partially pass into an amorphous state [52], as proven in Fig. 7(d). These results provide experimental evidence that phase transformation and amorphization may be another deformation mechanism in L-PBF AlSi10Mg alloy, in addition to dislocation slip, stacking faults and deformation twinning.

Conclusions

The AlSi10Mg samples containing multiple defects were successfully post-processed via ECAP, and the microstructures evolution was systematically investigated using electron microscopy and X-ray diffraction.

- EBSD analysis confirms that the ECAP samples exhibits heterogeneous deformation behaviour. Back stress, stacking faults, and occurrence of dynamic recrystallization enhanced the dislocation storage capacity of eutectic α-Al.
- The ultra-fine grained microstructure of L-PBF AlSi10Mg alloy was achieved through post-processing using qual channel angular pressing,
- X-ray diffraction and EBSD analysis proved a high dislocation density and the presence of GNDs concentration “hot spots” close to the Al/Si interfaces,
- Large quantity of different defects (i.e. dislocations, deformation twins, stacking faults and amorphous bands) were successfully identified using transmission electron microscopy,

Finally, the knowledge of the underlying micro-deformation mechanisms in L-PBF AlSi10Mg alloy described in this article will help us to develop novel strategies to modify the properties and improve the strength-ductility trade-off to produce lightweight components with superior properties.

Founding

The research was funded by the National Science Centre, Poland based on the decision number 2021/43/D/ST8/1946.
This research was completed in association with the project Innovative and additive manufacturing technology—new technological solutions for 3D printing of metals and composite materials, reg. no. 319 CZ.02.1.01/0.0/0.0/17_049/8 407, financed by Structural Funds of the European Union.

CRediT author statement

Przemysław Snopiński: Conceptualization, Methodology, Data curation, Data analysis, Investigation, Project Administration, Supervision, Writing - Original draft preparation, Funding acquisition **Ondrej Hilšer**: Methodology, Investigation, Resources, **Jiří Hajnyš**: Methodology, Investigation, Resources.

References

[1] K.-T. Żaba LechosławAU - Noga, PiotrAU - Rusz, StanislavAU - Zabystrzan, RostislavTI - Effect of Multi-Variant Thermal Treatment on Microstructure Evolution and Mechanical Properties of AlSi10Mg Processed by Direct Metal Laser Sintering and Casting, No Title, Materials (Basel). 15 (2022). https://doi.org/10.3390/ma15030974.

[2] B. Chen, S.K. Moon, X. Yao, G. Bi, J. Shen, J. Umeda, K. Kondoh, Strength and strain hardening of a selective laser melted AlSi10Mg alloy, Scr. Mater. (2017). https://doi.org/10.1016/j.scriptamat.2017.07.025.

[3] J. Wang, H. Yang, H. Huang, J. Zou, S. Ji, Z. Liu, High strength-ductility Co23Cr23Ni23Mn31 medium-entropy alloy achieved via defect engineering, Mater. Sci. Eng. A. 796 (2020) 139974. https://doi.org/https://doi.org/10.1016/j.msea.2020.139974.

[4] M. Liu, N. Takata, A. Suzuki, M. Kobashi, Development of gradient microstructure in the lattice structure of AlSi10Mg alloy fabricated by selective laser melting, J. Mater. Sci. Technol. 36 (2020) 106–117. https://doi.org/https://doi.org/10.1016/j.jmst.2019.06.015.

[5] Z. Liu, D. Zhao, P. Wang, M. Yan, C. Yang, Z. Chen, J. Lu, Z. Lu, Additive manufacturing of metals: Microstructure evolution and multistage control, J. Mater. Sci. Technol. 100 (2022) 224–236. https://doi.org/https://doi.org/10.1016/j.jmst.2021.06.011.

[6] R. Hadian, M. Emamy, N. Varahram, N. Nemati, The effect of Li on the tensile properties of cast Al-Mg2Si metal matrix composite, Mater. Sci. Eng. A. (2008). https://doi.org/10.1016/j.msea.2008.01.039.

[7] D. Zhang, Entwicklung des Selective Laser Melting ({SLM}) für Aluminiumwerkstoffe, Shaker, 2004. https://publications.rwth-aachen.de/record/52381.

[8] L. Wang, S. Wang, J. Wu, Experimental investigation on densification behavior and surface roughness of AlSi10Mg powders produced by selective laser melting, Opt. Laser Technol. 96 (2017) 88–96. https://doi.org/https://doi.org/10.1016/j.optlastec.2017.05.006.

[9] X. Li, D. Yi, X. Wu, J. Zhang, X. Yang, Z. Zhao, Y. Feng, J. Wang, P. Bai, B. Liu, Y. Liu, Effect of construction angles on microstructure and mechanical properties of AlSi10Mg alloy fabricated by selective laser melting, J. Alloys Compd. 881 (2021) 160459. https://doi.org/https://doi.org/10.1016/j.jallcom.2021.160459.

[10] A. Bin Anwar, Q.-C. Pham, Selective laser melting of AlSi10Mg: Effects of scan direction, part placement and inert gas flow velocity on tensile strength, J. Mater. Process. Technol. 240 (2017) 388–396. https://doi.org/https://doi.org/10.1016/j.jmatprotec.2016.10.015.

[11] M. Giovagnoli, M. Tocci, A. Fortini, M. Merlin, M. Ferroni, A. Migliori, A. Pola, Effect of different heat-treatment routes on the impact properties of an additively manufactured AlSi10Mg alloy, Mater. Sci. Eng. A. 802 (2021) 140671. https://doi.org/https://doi.org/10.1016/j.msea.2020.140671.

[12] B. Amir, E. Grinberg, Y. Gale, O. Sadot, S. Samuha, Influences of platform heating and post-processing stress relief treatment on the mechanical properties and microstructure of selective-laser-melted AlSi10Mg alloys, Mater. Sci. Eng. A. 822 (2021) 141612. https://doi.org/10.1016/J.MSEA.2021.141612.

[13] U. Patakham, A. Palasay, P. Wila, R. Tongsri, MPB characteristics and Si morphologies on mechanical properties and fracture behavior of SLM AlSi10Mg, Mater. Sci. Eng. A. 821 (2021) 141602. https://doi.org/10.1016/J.MSEA.2021.141602.

[14] A. Kempf, K. Hilgenberg, Influence of sub-cell structure on the mechanical properties of AlSi10Mg manufactured by laser powder bed fusion, Mater. Sci. Eng. A. 776 (2020) 138976. https://doi.org/10.1016/J.MSEA.2020.138976.

[15] Z. Li, Z. Li, Z. Tan, D.B. Xiong, Q. Guo, Stress relaxation and the cellular structure-dependence of plastic deformation in additively manufactured AlSi10Mg alloys, Int. J. Plast. 127 (2020) 102640. https://doi.org/10.1016/J.IJPLAS.2019.12.003.

[16] J. Merino, B. Ruvalcaba, J. Varela, E. Arrieta, L.E. Murr, R.B. Wicker, M. Benedict, F. Medina, Multiple, comparative heat treatment and aging schedules for controlling the microstructures and mechanical properties of laser powder bed fusion fabricated AlSi10Mg alloy, J. Mater. Res. Technol. 13 (2021) 669–685. https://doi.org/https://doi.org/10.1016/j.jmrt.2021.04.062.

[17] S.I. Shakil, A. Hadadzadeh, H. Pirgazi, M. Mohammadi, M. Haghshenas, Indentation-derived creep response of cast and laser powder bed fused AlSi10Mg alloy: Air temperature, Micron. 150 (2021) 103145. https://doi.org/https://doi.org/10.1016/j.micron.2021.103145.

[18] X.P. Li, X.J. Wang, M. Saunders, A. Suvorova, L.C. Zhang, Y.J. Liu, M.H. Fang, Z.H. Huang, T.B. Sercombe, A selective laser melting and solution heat treatment refined Al–12Si alloy with a controllable ultrafine eutectic microstructure

and 25% tensile ductility, Acta Mater. 95 (2015) 74–82. https://doi.org/https://doi.org/10.1016/j.actamat.2015.05.017.

[19] Z. Li, Z. Li, Z. Tan, D.B. Xiong, Q. Guo, Stress relaxation and the cellular structure-dependence of plastic deformation in additively manufactured AlSi10Mg alloys, Int. J. Plast. (2020). https://doi.org/10.1016/j.ijplas.2019.12.003.

[20] J. Li, J. Sun, Y. Li, G. Qian, Z. Wang, Very-high-cycle fatigue induced growth and amorphization of Si particles in additively manufactured AlSi10Mg alloy: Dependence of applied stress ratio, Int. J. Fatigue. 164 (2022) 107167. https://doi.org/https://doi.org/10.1016/j.ijfatigue.2022.107167.

[21] X.X. Zhang, H. Andrä, S. Harjo, W. Gong, T. Kawasaki, A. Lutz, M. Lahres, Quantifying internal strains, stresses, and dislocation density in additively manufactured AlSi10Mg during loading-unloading-reloading deformation, Mater. Des. (2021). https://doi.org/10.1016/j.matdes.2020.109339.

[22] Z. Zribi, H.H. Ktari, F. Herbst, V. Optasanu, N. Njah, EBSD, XRD and SRS characterization of a casting Al-7wt%Si alloy processed by equal channel angular extrusion: Dislocation density evaluation, Mater. Charact. (2019). https://doi.org/10.1016/j.matchar.2019.04.044.

[23] M. Liu, R. Zheng, W. Xiao, J. Li, G. Li, Q. Peng, C. Ma, Bulk nanostructured Al-Si alloy with remarkable improvement in strength and ductility, Scr. Mater. 201 (2021) 113970. https://doi.org/https://doi.org/10.1016/j.scriptamat.2021.113970.

[24] W. Li, S. Li, J. Liu, A. Zhang, Y. Zhou, Q. Wei, C. Yan, Y. Shi, Effect of heat treatment on AlSi10Mg alloy fabricated by selective laser melting: Microstructure evolution, mechanical properties and fracture mechanism, Mater. Sci. Eng. A. (2016). https://doi.org/10.1016/j.msea.2016.03.088.

[25] Z. Zhang, M.A. Cuddihy, F.P.E. Dunne, On rate-dependent polycrystal deformation: the temperature sensitivity of cold dwell fatigue., Proceedings. Math. Phys. Eng. Sci. 471 (2015) 20150214. https://doi.org/10.1098/rspa.2015.0214.

[26] G.K. Williamson, W.H. Hall, X-ray line broadening from filed aluminium and wolfram, Acta Metall. 1 (1953) 22–31. https://doi.org/http://dx.doi.org/10.1016/0001-6160(53)90006-6.

[27] K. Regina Cardoso, M.A. Muñoz-Morris, K. Valdés León, D.G. Morris, Room and high temperature ECAP processing of Al-10%Si alloy, Mater. Sci. Eng. A. (2013). https://doi.org/10.1016/j.msea.2013.09.006.

[28] Y. Tang, D. Xiao, L. Huang, R. You, X. Zhao, N. Lin, Y. Ma, W. Liu, Dynamic microstructural evolution of Al-Cu-Li alloys during hot deformation, Mater. Charact. 191 (2022) 112135. https://doi.org/https://doi.org/10.1016/j.matchar.2022.112135.

[29] N. Haghdadi, S. Primig, M. Annasamy, P. Cizek, P.D. Hodgson, D.M. Fabijanic, Dynamic recrystallization in AlXCoCrFeNi duplex high entropy alloys, J. Alloys Compd. 830 (2020) 154720. https://doi.org/https://doi.org/10.1016/j.jallcom.2020.154720.

[30] J. Chen, X. Jiang, L. Lyu, Y. Li, P. Christian, H. Sun, R. Shu, Microstructures and mechanical properties of nano-C and in situ Al2O3 reinforced aluminium matrix composites processed by equal-channel angular pressing, J. Alloys Compd. 876 (2021) 160159. https://doi.org/https://doi.org/10.1016/j.jallcom.2021.160159.

[31] K.J. Al-Fadhalah, M.K. Alyazidi, M. Rafiq, Effect of Microstructure Refinement on Hardness Homogeneity of Aluminum Alloy 1100 Processed by Accumulative Roll Bonding, J. Mater. Eng. Perform. 28 (2019) 4693–4706. https://doi.org/10.1007/s11665-019-04228-3.

[32] Y.-C. Wang, W. Zhang, L.-Y. Wang, Z. Zhuang, E. Ma, J. Li, Z.-W. Shan, In situ TEM study of deformation-induced crystalline-to-amorphous transition in silicon, NPG Asia Mater. 8 (2016) e291–e291. https://doi.org/10.1038/am.2016.92.

[33] G. Wu, J. Tang, N. Wang, Y. Cao, J. Luo, Y. Chen, Effect of strain rate-induced microstructure on mechanical

behavior of dual-phase steel, J. Mater. Res. Technol. 18 (2022) 2093–2103. https://doi.org/10.1016/J.JMRT.2022.03.123.

[34] R. Li, M. Wang, Z. Li, P. Cao, T. Yuan, H. Zhu, Developing a high-strength Al-Mg-Si-Sc-Zr alloy for selective laser melting: Crack-inhibiting and multiple strengthening mechanisms, Acta Mater. 193 (2020) 83–98. https://doi.org/10.1016/J.ACTAMAT.2020.03.060.

[35] S.I. Ahmed, K.A. Mkhoyan, K.M. Youssef, The activation of deformation mechanisms for improved tensile properties in nanocrystalline aluminum, Mater. Sci. Eng. A. 777 (2020) 139069. https://doi.org/10.1016/J.MSEA.2020.139069.

[36] Y.T. Zhu, X.Z. Liao, X.L. Wu, J. Narayan, Grain size effect on deformation twinning and detwinning, J. Mater. Sci. 48 (2013) 4467–4475. https://doi.org/10.1007/s10853-013-7140-0.

[37] Z. An, S. Mao, Y. Liu, L. Yang, A. Vayyala, X. Wei, C. Liu, C. Shi, H. Jin, C. Liu, J. Zhang, Z. Zhang, X. Han, Inherent and multiple strain hardening imparting synergistic ultrahigh strength and ductility in a low stacking faulted heterogeneous high-entropy alloy, Acta Mater. 243 (2023) 118516. https://doi.org/https://doi.org/10.1016/j.actamat.2022.118516.

[38] M.A. Meyers, A. Mishra, D.J. Benson, Mechanical properties of nanocrystalline materials, Prog. Mater. Sci. 51 (2006) 427–556. https://doi.org/10.1016/J.PMATSCI.2005.08.003.

[39] L. Wang, P. Guan, J. Teng, P. Liu, D. Chen, W. Xie, D. Kong, S. Zhang, T. Zhu, Z. Zhang, E. Ma, M. Chen, X. Han, New twinning route in face-centered cubic nanocrystalline metals, Nat. Commun. 8 (2017) 2142. https://doi.org/10.1038/s41467-017-02393-4.

[40] X. Shu, D. Kong, Y. Lu, H. Long, S. Sun, X. Sha, H. Zhou, Y. Chen, S. Mao, Y. Liu, Size effect on the deformation mechanisms of nanocrystalline platinum thin films, Sci. Rep. 7 (2017) 13264. https://doi.org/10.1038/s41598-017-13615-6.

[41] M. Wang, M. Knezevic, H. Gao, J. Wang, M. Kang, B. Sun, Phase interface induced stacking faults in Al-7.5Y alloy revealed by in-situ synchrotron X-ray diffraction and ex-situ electron microscopy, Mater. Charact. 179 (2021) 111322. https://doi.org/https://doi.org/10.1016/j.matchar.2021.111322.

[42] Q. Zeng, L. Wang, W. Jiang, Molecular Dynamics Simulations of the Tensile Mechanical Responses of Selective Laser-Melted Aluminum with Different Crystalline Forms, Crystals. 11 (2021). https://doi.org/10.3390/cryst11111388.

[43] B. Gwalani, M. Olszta, S. Varma, L. Li, A. Soulami, E. Kautz, S. Pathak, A. Rohatgi, P. V Sushko, S. Mathaudhu, C.A. Powell, A. Devaraj, Extreme shear-deformation-induced modification of defect structures and hierarchical microstructure in an Al–Si alloy, Commun. Mater. 1 (2020) 85. https://doi.org/10.1038/s43246-020-00087-x.

[44] M. Liu, H.J. Roven, Y. Yu, J.C. Werenskiold, Deformation structures in 6082 aluminium alloy after severe plastic deformation by equal-channel angular pressing, Mater. Sci. Eng. A. 483–484 (2008) 59–63. https://doi.org/10.1016/j.msea.2006.09.144.

[45] M.F. Ashby, The deformation of plastically non-homogeneous materials, Philos. Mag. (1970). https://doi.org/10.1080/14786437008238426.

[46] H. Idrissi, P. Carrez, P. Cordier, On amorphization as a deformation mechanism under high stresses, Curr. Opin. Solid State Mater. Sci. 26 (2022) 100976. https://doi.org/https://doi.org/10.1016/j.cossms.2021.100976.

[47] S.K. Mohapatra, V. Ranjan, S. Tripathy, Study of severe plastic deformations of metallic materials:- A move towards Amorphization, Mater. Today Proc. 56 (2022) 735–741. https://doi.org/https://doi.org/10.1016/j.matpr.2022.02.244.

[48] S. Jiang, R.L. Peng, N. Jia, X. Zhao, L. Zuo, Microstructural and textural evolutions in multilayered Ti/Cu composites

processed by accumulative roll bonding, J. Mater. Sci. Technol. 35 (2019) 1165–1174. https://doi.org/https://doi.org/10.1016/j.jmst.2018.12.018.

[49] S. Bhattacharya, A.R. Riahi, A.T. Alpas, Indentation-induced subsurface damage in silicon particles of Al–Si alloys, Mater. Sci. Eng. A. 527 (2009) 387–396. https://doi.org/10.1016/J.MSEA.2009.08.052.

[50] O. Shikimaka, A. Prisacaru, Deformation mechanisms under nanoscratching of Si: effect of scratching speed, load and indenter orientation, Mater. Res. Express. 6 (2019) 85011. https://doi.org/10.1088/2053-1591/ab1a0d.

[51] T.D. Shen, C.C. Koch, T.L. McCormick, R.J. Nemanich, J.Y. Huang, J.G. Huang, The structure and property characteristics of amorphous/nanocrystalline silicon produced by ball milling, J. Mater. Res. 10 (1995) 139–148. https://doi.org/10.1557/JMR.1995.0139.

[52] R. V Sundeev, A. V Shalimova, A.M. Glezer, E.A. Pechina, M. V Gorshenkov, G.I. Nosova, In situ observation of the “crystalline⇒amorphous state” phase transformation in Ti2NiCu upon high-pressure torsion, Mater. Sci. Eng. A. 679 (2017) 1–6. https://doi.org/https://doi.org/10.1016/j.msea.2016.10.028.